2011

Neutrally buoyant particle dynamics in fluid flows: Comparison of experiments with Lagrangian stochastic models

Themistoklis P. Sapsis

Nicholas T. Ouellette

Jerry P. Gollub
Haverford College

George Haller

Neutrally buoyant particle dynamics in fluid flows: Comparison of experiments with Lagrangian stochastic models

Themistoklis P. Sapsis, Nicholas T. Ouellette, Jerry P. Gollub, and George Haller

Related Articles

Additional information on Phys. Fluids

Neutrally buoyant particle dynamics in fluid flows: Comparison of experiments with Lagrangian stochastic models

Themistoklis P. Sapsis,[1,a)] Nicholas T. Ouellette,[2,b)] Jerry P. Gollub,[3,c)] and George Haller[4,d)]

[1]*Department of Mechanical Engineering, Massachusetts Institute of Technology, Cambridge, Massachusetts 02139, USA*
[2]*Department of Mechanical Engineering & Materials Science, Yale University, New Haven, Connecticut 06520, USA*
[3]*Department of Physics, Haverford College, Haverford, Pennsylvania 19041, USA*
[4]*Department of Mechanical Engineering, and Department of Mathematics and Statistics, McGill University, Montreal, Quebec H3A 2K6, Canada*

We study the validity of various models for the dynamics of finite-sized particles in fluids by means of a direct comparison between theory and experimentally measured trajectories and velocities of large numbers of particles in chaotic two-dimensional flow. Our analysis indicates that finite-sized particles follow the predicted particle dynamics given by the Maxey-Riley equation, except for random correlated fluctuations that are not captured by deterministic terms in the equations of motion, such as the Basset-Boussinesq term or the lift force. We describe the fluctuations via spectral methods and we propose three different Lagrangian stochastic models to account for them. These Lagrangian models are stochastic generalizations of the Maxey-Riley equation with coefficients calibrated to the experimental data. We find that one of them is capable of describing the observed fluctuations fairly well, while it also predicts a drag coefficient in near agreement with the theoretical Stokes drag. © 2011 American Institute of Physics. [doi:10.1063/1.3632100]

I. INTRODUCTION

Inertial (or finite-sized) particles are commonly encountered in natural phenomena and industrial processes. Examples of inertial particles include dust, impurities, droplets, and air bubbles, with important applications in pollutant transport in the ocean and atmosphere,[1–3] rain initiation,[4–6] coexistence between plankton species in the hydrosphere,[7,8] and planet formation by dust accretion in the solar system.[9–12]

The theoretical analysis of inertial particle motion apparently started with the work of Stokes,[13] who addressed the motion of an isolated sedimenting particle in a fluid for the case where the inertia of the flow is negligible, the flow field being totally dominated by viscous diffusion. However, as was shown by Oseen,[14] neglecting the nonlinear terms in Navier-Stokes equations leads to serious discrepancies in regions away from the particle. Oseen preserved one of the convective terms in the Navier-Stokes equations to obtain an $\mathcal{O}(\text{Re})$ solution for the drag force. Proudman and Pearson,[15] with a later extension by Sano,[16] used multi-scale asymptotic analysis to obtain an elegant $\mathcal{O}(\text{Re} \ln(\text{Re}))$ solution for the drag force. Saffman[17] studied the shear-induced lift that originates from the inertial effects in the viscous flow around the particle and obtained an analytical expression for its description. Basset[18] identified a memory-like contribution to the drag on a particle, which depends on the history of the motion of the particle and on the viscosity of the fluid (see also Mordant and Pinton[19] for an experimental illustration of this memory term).

Lawrence and Mei[20] were concerned with the long-time behavior of impulsive motions of particles in fluids. Maxey and Riley[21] carried out a complete analysis of the motion of a sphere in unsteady Stokes flow for nonuniform flow fields and derived a governing equation for the relative velocity of the particle for any given nonuniform transient background flow. This included additional terms associated with relative accelerations and Faxén's correction.

Parallel to all these theoretical studies, a number of experiments have been conducted to describe the acceleration statistics of neutrally buoyant inertial particles. Qureshi *et al.*,[22] Brown *et al.*,[23] and Voth *et al.*[24] studied the Lagrangian statistics of such particles experimentally studied in isotropic turbulence with Taylor-microscale Reynolds numbers of $140 < R_\lambda < 970$. Calzavarini *et al.*[25] showed that for larger particles, the consideration of Faxén's correction improves the comparison between the statistics produced by direct numerical simulations and experimental measurements in turbulent flows. Finally, Ouellette *et al.*[26] studied neutrally buoyant particles in a spatiotemporally chaotic flow by simultaneously measuring the flow field and the trajectories of millimeter scale particles, so that the two could be directly compared.

In the present paper, we seek to compare experimental results with available theoretical models of *individual inertial particle trajectories*. More specifically, we compare inertial particle motions in the experiments of Ouellette *et al.*[26] to those predicted by the full Maxey-Riley equation.

Since the particles in the experiment are small, their motion is expected to stay close to the motion of infinitesimal fluid elements over short time intervals. Verifying this by

a)Electronic mail: sapsis@mit.edu.
b)Electronic mail: nicholas.ouellette@yale.edu.
c)Electronic mail: jgollub@haverford.edu.
d)Electronic mail: george.haller@mcgill.ca.

itself, however, would simply verify a basic physical expectation rather than a dynamical model for inertial particle motion. To go beyond this, we seek to observe experimentally a specific dynamical feature predicted by the Maxey-Riley equation for neutrally buoyant inertial particles: their exponentially fast synchronization with the motion of fluid elements, as evidenced by the rapid alignment of neutrally buoyant inertial particle velocities with the ambient fluid flow velocity.

The full Maxey-Riley equations include integral terms with singular kernels, which requires the use of novel numerical schemes in order to generate accurate particle trajectories. Once the Maxey-Riley trajectories are obtained, we use analytical and numerical tools to assess the impact of the various dynamical terms (drag force, lift force, etc.) on particle motion. We find that the experimentally observed particle velocities show persistent fluctuations relative to the ambient fluid velocities. Consideration of the Basset-Boussinesq term or the lift force in the modeling equations significantly affects the velocity of the particles but does not reduce the size of the fluctuations, which have a strongly stochastic character with narrow banded spectra (i.e., strongly correlated statistics) that cannot be characterized as experimental noise.

We present and compare three stochastic models for describing the differences between theory and observation. These Lagrangian models are stochastic generalizations of the Maxey-Riley equation having unknown coefficients which are determined by identifying experimental and theoretical statistical descriptors, such as the correlation time-scale, the spectrum, or the shape of the tail of the probability density of the velocity fluctuations. Among these three models, we find that the one based on the identification of the full spectrum of the random fluctuations produces better qualitative agreement with the experimentally observed fluctuations than the others, while it also predicts a drag coefficient that is in near agreement with the theoretical Stokes drag. Hence, with this spectral based stochastic approach, we are able to model efficiently the experimentally observed fluctuations of the velocity of finite-size particles that cannot be captured by the deterministic terms in the Maxey-Riley equation.

II. EXPERIMENTAL FLOW

The experimental flow field is generated by driving a thin layer of an electrolytic fluid electromagnetically (see Ouellette and Gollub[27] for a detailed description). The resulting flow is quasi-two-dimensional, since there is essentially no fluid motion in the depth direction. The Reynolds number is given by $\mathrm{Re} = UL/v$, where U is the root-mean-square velocity, $L = 2.54$ cm is the characteristic length of the flow, taken to be the magnet spacing, and v is the kinematic viscosity. In our experiments, $72 \leq \mathrm{Re} \leq 220$, which is above the transition to spatiotemporal chaos for this flow (see Ouellette and Gollub[28]). All the results and equations that follow are non-dimensionalized using the characteristic velocity U and the characteristic length L.

A. Flow measurement

To measure the flow experimentally, we use neutrally buoyant tracers with a diameter of $d = 80~\mu$m. To avoid any surface-tension-driven interactions between the particles, we place a 3.5-mm-deep layer of water above the electrolytic fluid; the particles lie at the interface between the two layers and, since those are miscible, there is no bulk surface tension between them (see Vella and Mahadevan[29]).

We image the particles at a rate of 20 Hz and with a precision of approximately 13 μm (0.1 pixels). To avoid boundary effects, we focus on the 7.5 cm $\times$ 7.5 cm region in the center of the flow. We extract the velocity and acceleration of each particle using polynomial fits to short track sections. To resolve the flow field well, we use a large number of tracers (roughly 15 000); even with this large number of particles, however, the loading density is sufficiently small so that interactions between the particles are negligible.

Using a Delaunay-triangulation-based linear interpolation scheme, we obtain a first approximation of the velocity field by interpolating between the discrete particle velocities. We then apply a moving-average spatial smoothing (20 pixels wide) for each time step. Next, we interpolate back to the original positions of the tracers to estimate their velocity from the smoothed velocity field. By comparing the originally measured velocity of each tracer particle with the estimate from the interpolation of the smooth velocity field, we perform a consistency check and reject tracer particles that have larger discrepancy than the root-mean-square velocity U (Fig. 1). Some discrepancy (due to a small number of tracking errors) is unavoidable; these errors are easily correctable, however, since the velocity fluctuations should be Gaussian in this Reynolds number range. We emphasize that in rejecting these particles, we do not exclude inertial particles that diverge from the flow field; such inertial particles are not used in reconstructing the flow field. Finally, we repeat the reconstruction procedure without the tracer particles that were rejected from the consistency check and perform spatial averaging in both space and time using the moving-average method (20 pixels wide in space and 5 frames in time).

B. Removal of flow divergence

While the physical flow is expected to be nearly incompressible in the plane (since our measurements are made far from the lateral side walls of the apparatus), the reconstructed velocity field $\mathbf{u}(\mathbf{x},t)$ admits regions of non-negligible divergence (see Fig. 1), indicating errors in the reconstruction.

In Fig. 2(b), we show the divergence field

$$\mathcal{C}(\mathbf{x},t) = \mathrm{div}\,\mathbf{u}(\mathbf{x},t),$$

with clearly visible regions of nonzero divergence. To address these errors, we represent the flow field $\mathbf{u}(\mathbf{x},t)$ as a sum of a solenoidal and an irrotational fields (cf., Batchelor),[30]

$$\mathbf{u}(\mathbf{x},t) = \mathbf{u}_I(\mathbf{x},t) + \mathbf{u}_S(\mathbf{x},t) = \nabla\varphi + \nabla \times \psi. \qquad (1)$$

The divergence of the flow is then exclusively due to the irrotational term $\mathbf{u}_I(\mathbf{x},t)$, because

$$\mathrm{div}\,\mathbf{u} = \mathrm{div}\,\mathbf{u}_I(\mathbf{x},t) + \mathrm{div}\,\mathbf{u}_S(\mathbf{x},t) = \mathrm{div}\,\mathbf{u}_I(\mathbf{x},t) = \Delta\varphi.$$

To determine the unknown potential ϕ in Eq. (1), we numerically solve Eq. (1) as a Poisson equation with homogeneous
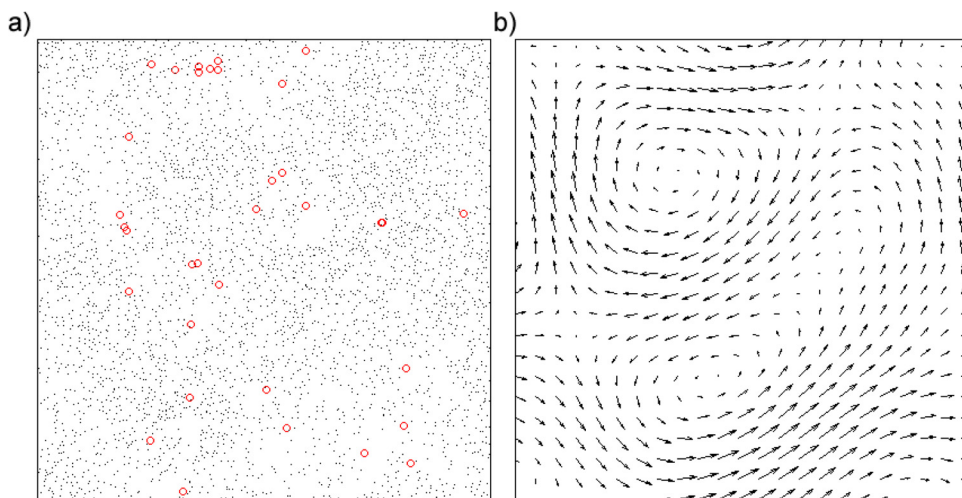
a)

b)

FIG. 1. (Color online) (a) Black circles: tracer particles used for the reconstruction of the velocity field; lighter circles (red): rejected particles. (b) Computed velocity field $\mathbf{u}(\mathbf{x},t)$ for Re = 185.

Neumann boundary conditions. The boundary conditions express the fact that the flow near the edges is exclusively due to the vorticity field. As a result of this procedure, we have the following incompressible velocity field:

$$\hat{\mathbf{u}}(\mathbf{x},t) = \mathbf{u}(\mathbf{x},t) - \nabla\varphi,$$

that has a vorticity field identical to the original flow, since

$$\operatorname{curl} \hat{\mathbf{u}}(\mathbf{x},t) = \operatorname{curl} \mathbf{u}(\mathbf{x},t) - \operatorname{curl} \nabla\varphi = \operatorname{curl} \mathbf{u}(\mathbf{x},t).$$

The results of this approach are shown in Fig. 2. As seen in the figure, the vorticity field of the original (a) and the resulting flow (c) are indistinguishable, while the latter has very small divergence (Figure 2(d)). Specifically, we have $\int ||\nabla\varphi||^2 dx < 0.002 \int ||\mathbf{u}||^2 dx$ over the time interval that we

consider for our studies. Thus, this modification does not change the characteristics of the flow but only improves the consistency of the u and v components reducing further the experimental errors.

III. THE GENERALIZED MAXEY–RILEY EQUATION

In this section, we use the experimentally measured velocity field and the experimentally measured trajectories of larger particles placed in the same flow to evaluate a generalized deterministic model for the dynamics of finite-sized particles. The larger particles are of diameter $d = 0.92$ mm and their Stokes number is in the range $0.53 \times 10^{-2} \le St \le 1.6 \times 10^{-2}$. We denote that their non-dimensional radius by a, their density by ρ_p, and the fluid density by ρ_f.

a)

b)

c)

d)
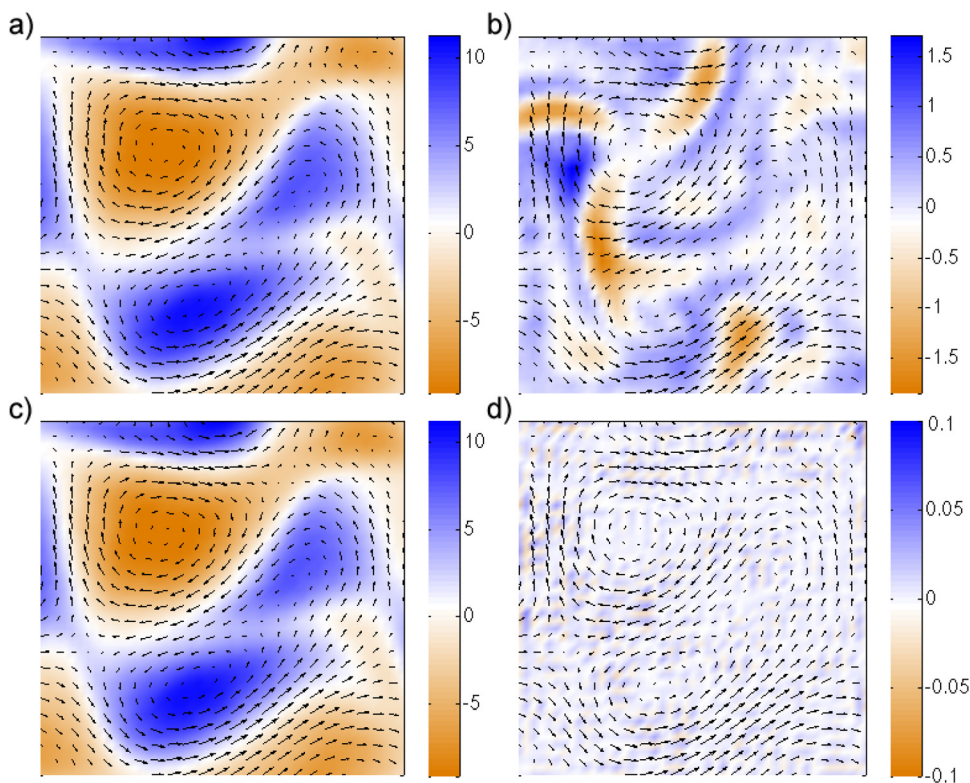

FIG. 2. (Color online) (a)-(b) Vorticity field (curl $\mathbf{u}$) and divergence field (div $\mathbf{u}$), respectively, before the application of the divergence removal algorithm. (c)-(d) Resulting vorticity field (curl $\mathbf{u}$) and divergence field (div $\mathbf{u}$), respectively (Re = 185).

Let the material derivative be denoted as

$$\frac{D\mathbf{u}}{Dt} = \mathbf{u}_t + (\nabla\mathbf{u})\mathbf{u},$$

where ∇ denotes the gradient operator with respect to $\mathbf{x}$. Provided that the particle is spherical and that the relative-velocity Reynolds number is small, that is,

$$\mathrm{Re}_r = 2aUL|\mathbf{v} - \mathbf{u}|/\nu = 2a\mathrm{Re}|\mathbf{v} - \mathbf{u}| \ll 1, \qquad (2)$$

the particle velocity $\mathbf{v}(t) = \underline{\mathbf{x}}(t)$ satisfies the generalized Maxey-Riley equation of motion (cf., Henderson[31])

$$\dot{\mathbf{v}} = \frac{3R}{2}\frac{D\mathbf{u}}{Dt} + \left(1 - \frac{3R}{2}\right)\mathbf{g} - \frac{R}{St}\left(\mathbf{v} - \mathbf{u} - \frac{a^2}{6}\Delta\mathbf{u}\right) + \frac{R}{2}\frac{a^2}{10}\frac{D}{Dt}\Delta\mathbf{u}$$
$$- R\sqrt{\frac{9}{2\pi}}\sqrt{\frac{1}{St}}\int_0^t \frac{1}{\sqrt{t-s}}\left[\dot{\mathbf{v}}(s) - \frac{d}{ds}\left(\mathbf{u} + \frac{a^2}{6}\Delta\mathbf{u}\right)_{\mathbf{x}=\mathbf{x}(s)}\right]ds$$
$$+ \frac{6.46R}{\frac{4}{3}\pi a}\sqrt{\frac{1}{\mathrm{Re}|\omega|}}(\mathbf{v} - \mathbf{u}) \times \omega, \qquad (3)$$

where $R = \frac{2\rho_f}{\rho_f + 2\rho_p}$ is the density ratio that distinguishes neutrally buoyant particles ($R = 2/3$) from aerosols ($0 < R < 2/3$) and bubbles ($2/3 < R < 2$), $\mathbf{g}$ is the constant gravitational acceleration vector, v is the kinematic viscosity of the fluid, and $\omega = \mathrm{curl}\,\mathbf{u}$ is the local flow vorticity. We have also used the Stokes and Reynolds numbers defined as

$$St = \frac{2}{9}a^2\mathrm{Re}, \qquad \mathrm{Re} = UL/\nu.$$

The individual force terms listed in separate lines on the right-hand side of Eq. (3) have the following physical meaning: (1) force exerted on the particle by the undisturbed flow, (2) buoyancy force, (3) Stokes drag, (4) added-mass term resulting from the part of the fluid moving with the particle, (5) Basset–Boussinesq memory term, and (6) lift force due to flow vorticity. The terms involving $a^2\Delta\mathbf{u}$ are usually referred to as the Faxén corrections.

Motivated by the experiments of Ouellette and Gollub,[28] we consider the case of neutrally buoyant particles. First, we set $R = 2/3$ and perform the change of variables $\mathbf{z} = \mathbf{v} - \mathbf{u}$ in Eq. (3) to obtain

$$\dot{\mathbf{z}} + \sqrt{\frac{2}{\pi St}}\int_0^t \frac{\dot{\mathbf{z}}(s)}{\sqrt{t-s}}ds$$
$$= -\left[\nabla\mathbf{u} + \frac{1}{3}\frac{a^2}{10}(\nabla(\Delta\mathbf{u})) + \frac{2}{3St}\mathbf{I}\right]\mathbf{z}$$
$$+ \frac{6.46}{2\pi a}\sqrt{\frac{1}{\mathrm{Re}|\omega|}}\mathbf{z} \times \omega + \frac{1}{3}\frac{a^2}{10}\frac{d}{dt}\Delta\mathbf{u} + \frac{a^2}{9St}\Delta\mathbf{u}$$
$$+ \frac{a^2}{6}\sqrt{\frac{2}{\pi St}}\int_0^t \frac{1}{\sqrt{t-s}}\frac{d}{ds}\left[(\Delta\mathbf{u})_{\mathbf{x}=\mathbf{x}(s)}\right]ds. \qquad (4)$$

Next, we compute the relative-velocity Reynolds number Re_r (defined in Eq. (2)) of the particles. We use the experimental measurements for the large particle velocity as well as the computed flow field in order to calculate the magnitude of the quantity $|\mathbf{v} - \mathbf{u}|$ using its standard deviation. The
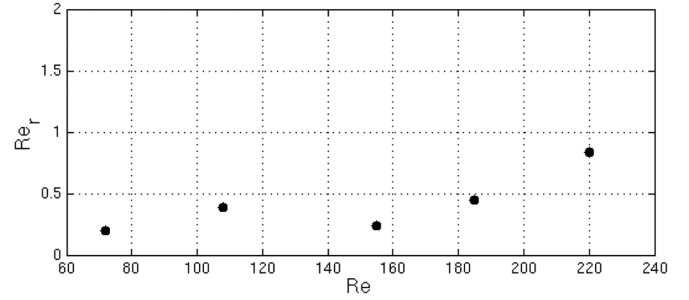

FIG. 3. Particle relative velocity Reynolds number Re_r with respect to the flow Reynolds number.

computed values of Re_r are shown in Figure 3; we note that the assumption of small relative-velocity Reynolds number in the derivation of Eq. (4) (cf., Maxey[21]) is satisfied for the most Reynolds numbers except the last one, where Re_r is close to one. Therefore, we expect that at least for the first four flow Reynolds numbers, Eq. (4) describes the experimentally measured dynamics adequately.

In the absence of the Faxén corrections (last line of Eq. (4)), the two-dimensional plane $\{\mathbf{z} = \mathbf{0}\}$ is an invariant manifold for Eq. (4). Faxén corrections are the only terms that can cause a divergence from this manifold. However, their small magnitude (they are proportional to a^2) indicates that a divergence from the invariant manifold should also be the result of an instability of the state $\{\mathbf{z} = \mathbf{0}\}$. This discussion leads us to study the stability of the invariant manifold. For the case where $a/\sqrt{\tilde{\nu}} \ll 1$ (where $\tilde{\nu} = \frac{\nu}{UL}$ is the non-dimensional viscosity) is very small (or equivalently in dimensional form $d\sqrt{U} \ll 2\sqrt{L\nu}$), we may neglect the Basset–Boussinesq and the lift force term in Eq. (4) to obtain the simplified equation of motion (Maxey-Riley equation)

$$\dot{\mathbf{z}} + \left[\nabla\mathbf{u} + \frac{2}{3St}\mathbf{I}\right]\mathbf{z} = \mathbf{0}. \qquad (5)$$

Even though simple in form, the above equation may produce inertial particle trajectories that differ completely from those of infinitesimal fluid elements (due to dynamical instabilities).[32] The stability of Eq. (5) was studied by Sapsis and Haller[33] where it was proved that the $z = 0$ plane is attracting if and only if

$$s(\mathbf{x}, t) = \lambda_{\max}\left[\frac{\nabla\mathbf{u}(\mathbf{x}, t) + [\nabla\mathbf{u}(\mathbf{x}, t)]^T}{2}\right] - \frac{2}{3St} < 0 \quad (6)$$

hold for all $\mathbf{x}$ and t in the domain of interest. In Fig. 4(b), we present the stability indicator $s(\mathbf{x}, t)$ for the finite-sized particles moving in a flow with $\mathrm{Re} = 185$. As seen from the figure, we have global stability of the $\mathbf{z} = \mathbf{0}$ invariant plane of Eq. (5). Consequently, Eq. (4) without the Basset–Boussinesq memory term, the lift force term, and the Faxén corrections predicts a rapid convergence of the particles to the flow velocity field and, therefore, cannot capture the fluctuations that we observe experimentally. These results are also verified by the direct numerical simulation of Eq. (5) (Fig. 4(d)) for the large particle velocity fluctuation along the experimentally measured path $\mathbf{x}_p(t)$ of each finite-sized particle p (Fig. 4(a)).
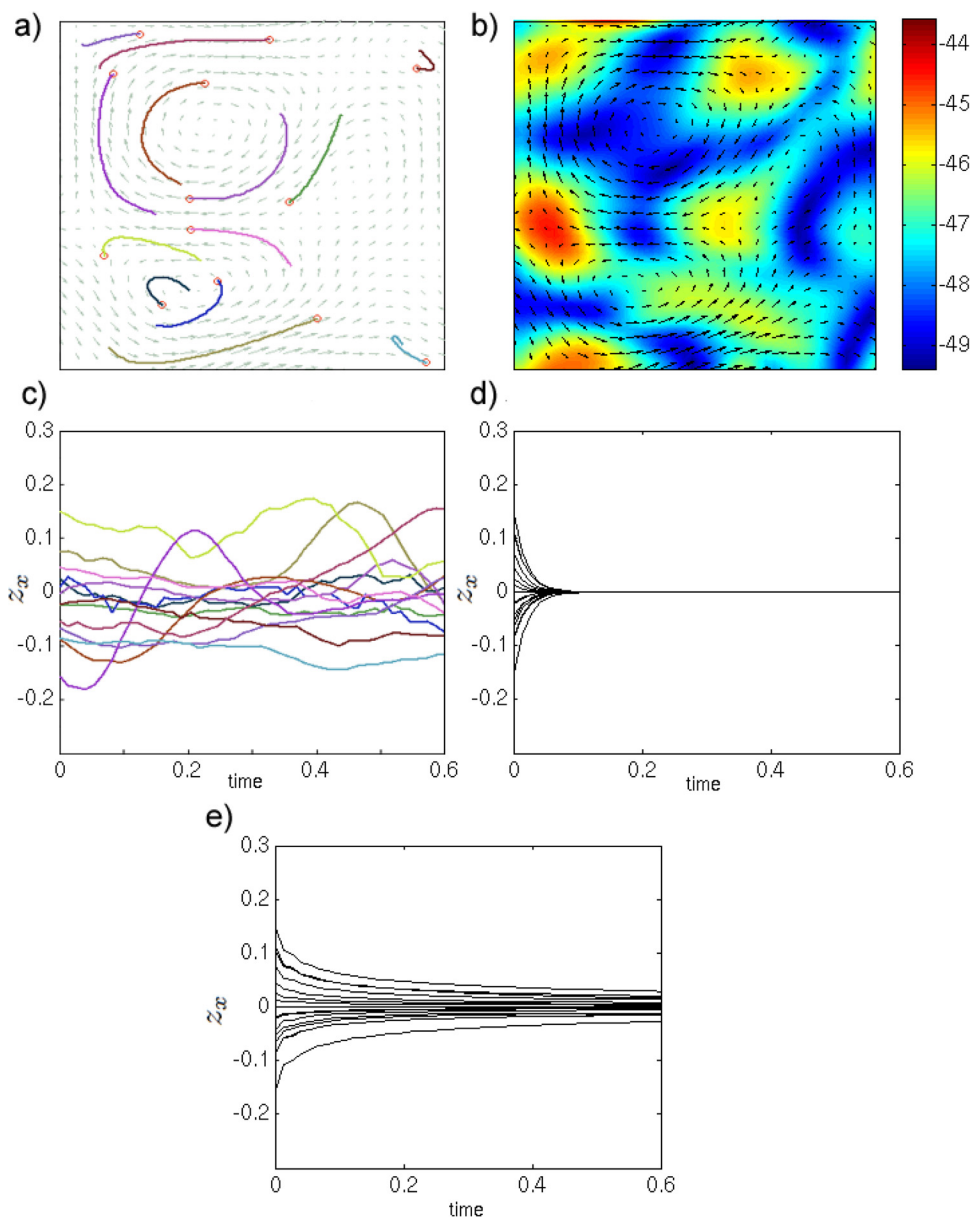
FIG. 4. (Color online) Finite-size particles in the flow with Re = 185. (a) Particle trajectories and instantaneous velocity field. (b) Stability indicator $s(\mathbf{x},t)$. (c) Fluctuations of the x-velocity component measured directly from the experiment (colored/shaded in accordance to (a)). (d) Fluctuations of the x-velocity component computed from the Maxey-Riley Equation (5). (e) Fluctuations of the x-velocity component computed from the generalized Maxey-Riley Equation (4).

The next step of our analysis involves the stability of the state $\{\mathbf{z} = \mathbf{0}\}$ for the full Equation (4). Due to the infinite-dimensional character of this equation, we study its stability properties numerically. However, even the numerical solution of Eq. (4) presents important difficulties since it involves the computation of an integral quantity with a singular kernel. In Mechaelides,[34] a transformation of the equation of motion is obtained in which the velocity of the sphere does not appear in the history integral. Even in this case, however, we still need to compute a generalized integral involving a singular kernel. Various other numerical methods have been developed for the efficient solution of Eq. (4), including methods based on suitable approximation of the tail of the Basset term[35] and on fractional derivatives[36] (see Alexander[37] for a classification of various solution alternatives together with their advantages and drawbacks).

Here, we use a variant of the method presented in Alexander[37] based on a central-difference scheme that is suitably modified to treat the generalized integral term. The

details of this numerical algorithm are given in the Appendix. A sufficiently small timestep was used in order to obtain a numerical convergence. As in the case of Eq. (5), we use the experimentally measured path of each finite-sized particle, so that we do not have errors in our calculations due to position differences. Our analysis indicates that, in the absence of the Faxén corrections, the invariant manifold $\{\mathbf{z}=\mathbf{0}\}$ is stable over all relative velocity Reynolds number Re_r. The inclusion of the Faxén terms caused negligible difference on the velocity of the large particles as it is expected given the small magnitude of those terms and the stability properties of the invariant manifold.

We emphasize that the consideration of the integral term in our analysis, resulted in an important difference on the velocity of the particle (consistently with the conclusions of Mei et al.[38] and Armenio et al.[39]) although it did not improve the agreement with the experimental observations. This is shown in Fig. 4(e) where we present numerical simulations of the x-component of the particle velocity fluctuation

z (z_x denotes the x-component) using the generalized Equation (4) for flow Reynolds number, Re = 185. In contrary to the velocity fluctuation computed using the Maxey-Riley Equation (5), the velocity fluctuation decays much slower in this case. Moreover, a comparison of Fig. 4(e) with the experimental observations (Fig. 4(c)) shows that the inclusion of the Basset–Boussinesq memory term, the lift force term, and the Faxén corrections still does not explain the persistent oscillations around the solution $z = 0$ observed in the experimental particle trajectories (Fig. 4(c)). Although in principle other terms could be added, they must all be small (given the assumptions of the Maxey-Riley equations), and so they will not change the character of the equations, even if they change the details. As an example of this, note the difference between the results in Fig. 4, panels (d) and (e), adding more terms to the Maxey-Riley equations changes the quantitative details but not the qualitative dynamics. Thus, adding more deterministic terms to the Maxey-Riley equations cannot reproduce the experimental fluctuations we observe in, for example, Fig. 4(c). The stochastic character of these fluctuations leads us to consider adding terms to the Maxey-Riley equations to explain the random features observed in the experiment.

IV. STATISTICAL DESCRIPTION OF VELOCITY FLUCTUATIONS

In this section, we give a detailed description of the velocity fluctuations of the finite-sized particles away from the underlying flow field. These fluctuations have a strongly random character and cannot be captured by the deterministic terms of the Maxey-Riley equation. We denote the measured velocity of the particle by $\mathbf{v}_p(t)$. We then define the velocity difference $\mathbf{z}_p(t) = \mathbf{v}_p(t) - \mathbf{u}(\mathbf{x}_p(t), t)$ along the particle trajectory.

By direct numerical computation, we observe that the global mean (averaging over particles and time) of the velocity fluctuations is negligible relative to the characteristic size of the fluctuations. Subsequently, we compute the spectrum defined as the power spectrum of the time series for the velocity fluctuations averaged over particles. In Fig. 5, we show the power spectrum (dark curve—blue) for different flow Reynolds numbers. We observe in all cases that the spectrum decays quickly (i.e., the stochasticity occurs at low frequencies), and therefore, the observed fluctuations cannot be due to experimental noise.

More likely causes of these discrepancies are reconstruction errors in the flow velocity field and neglected dynamical effects in the modeling equations, such as interaction of the boundary layers behind the particles or three-dimensional flow-particle effects; however, three-dimensional effects cannot be quantified in our two-dimensional experimental setup. A statistical analysis of the large particle velocity fluctuations and the spatial density of the small tracers (those used for the measurement of the flow) around its instantaneous location reveals partial correlation between the locations of low density of tracers and neighborhoods where large fluctuations are observed. Specifically, computing the correlation coefficient σ between the local density of small particles and the magnitude of the velocity fluctuations of the large particles, we find

for a typical dataset ($Re = 185$) that $\sigma = -25.84\%$. This modest anticorrelation shows that the regions of higher tracer particle density fluctuate less strongly, indicating that reconstruction errors are at least partly responsible for the observed discrepancies. The statistical significance of these quantities is also indicated by a very small p-value (order of 10^{-18}). We note that an explanation of this nature (i.e., errors in the reconstructed flow field) is compatible with the narrow-banded character of the fluctuations, since the error is not restricted in an infinitesimally small neighborhood but rather extends into a finite area causing the particle to experience velocity fluctuations with larger memory (or correlation time scale), which is equivalent to the observed narrow-banded spectrum.

From the previous analysis, we also conclude that important velocity fluctuations of the large particles do not have significant correlation with regions of the flow characterized by a large number of flow measurement tracers; this validates our initial hypothesis that interaction among particles is negligible and does not change the dynamics. Moreover, the small scale of these interactions, if they were present, would lead to spatially uncorrelated error, i.e., error in the flow field that has very small spatial correlation scale, causing only fluctuations with small memory or a wide-banded spectrum, which would be incompatible with the observed one.

We now provide a dynamical characterization of the observed statistics. To this end, we first use the following spectral representation that adequately approximates the experimentally measured spectrum over the range of Reynolds numbers considered:

$$S_{zz}(\omega) = \frac{1}{a_1\omega^4 + a_2\omega^2 + a_3}. \tag{7}$$

We obtain the unknown coefficients by least-squares optimization; the resulting approximation is shown in Fig. 5 as a light curve (red). The next step of our analysis involves the computation of the correlation time scale that defines the time interval after which fluctuations are considered uncorrelated. This computation is based directly on the spectrum of the stochastic process. Specifically, the covariance function $C_{zz}(\tau)$ may be obtained as the inverse Fourier transform of the power spectrum $S_{zz}(\omega)$. Then, the correlation time scale is defined in terms of the covariance function as (see, e.g., Sobczyk)[40]

$$\tau_z = C_{zz}^{-1}(0) \int_0^\infty C_{zz}(\tau)d\tau. $$

We present the computed correlation time scale in terms of the flow Reynolds number in Fig. 6. Despite the increased value of the correlation time scale that corresponds to the largest Re value, most of the points present a decaying trend as the flow Reynolds increases; an indication that, for larger Reynolds, the particle dynamics depends less on the history of the particle's trajectory. Finally, we characterize the probability density function (pdf) of the velocity fluctuations. In order to have statistically independent fluctuations, we
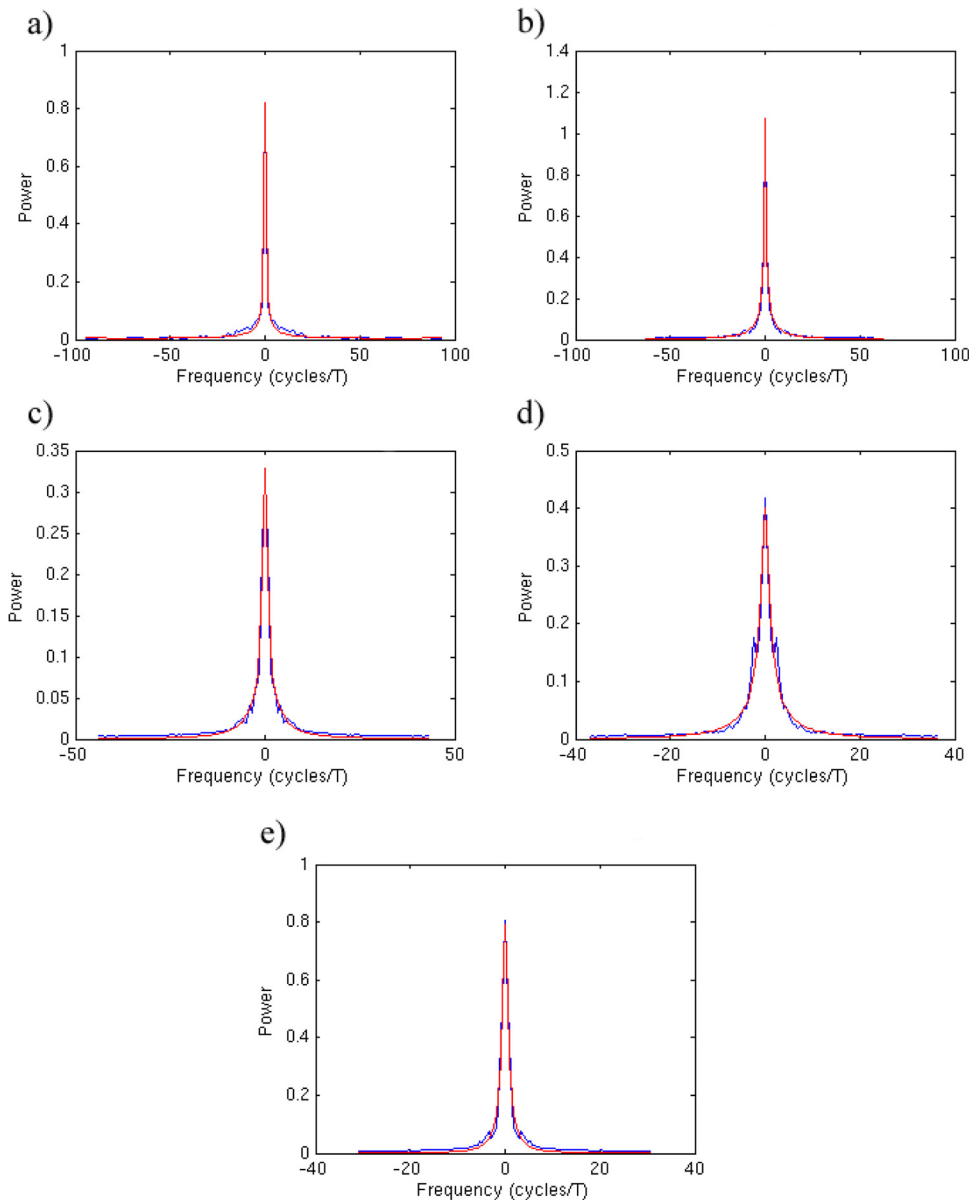
a)

b)

c)

d)

FIG. 5. (Color online) Power spectrum for velocity fluctuations at different flow Reynolds numbers: Re = 72 (a), 108 (b), 155 (c), 185 (d), and 220 (e); dark curve (blue): experimentally measured; light curve (red): analytical approximation.

e)

sample the velocity time series at time instants t_i, $i = 1,2,\ldots$ having distance $|t_{i+1} - t_i|$ larger than the correlation time scale τ_z computed previously. Then we may define the probability density function as

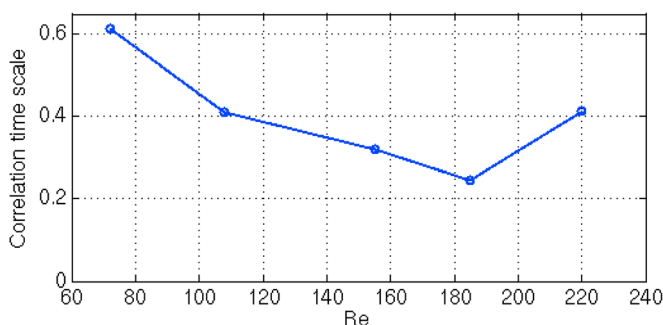$$f_{z_x}(x) = \frac{d}{dx}\mathcal{P}\{z_{x,p}(t_i) \leq x; |t_{i+1} - t_i| > \tau_z\},$$

FIG. 6. (Color online) Correlation time scale for velocity fluctuations as a function of the flow Reynolds number.

where $\mathcal{P}$ denotes the probability of the event in the brackets. In Fig. 8(a), we present the standard deviation σ_{z_x} of the velocity fluctuations as a function of the Reynolds number of the flow and we observe that the magnitude of the velocity fluctuations is approximately 5%-10% of the characteristic flow velocity.

For finite-sized particle dynamics, the shape of the pdf plays an important role, since, in general, the statistics are not Gaussian and the distributions are heavy-tailed. To quantify this non-Gaussian behavior, we define the tail-coefficient of the pdf as the positive real number α for which

$$f_{z_x}(x) \propto |x|^{-\alpha} \text{ for large } |x|. \tag{8}$$

To estimate the above coefficient, we use a maximum likelihood method that gives the best-fit power law exponent for a series of N observations $z_{x,p}(t_i)$ as

$$\alpha = 1 + N\left[\sum_p \sum_i \ln\left(\frac{z_{x,p}(t_i)}{z_{x,\min}}\right)\right]^{-1}, \tag{9}$$

where $z_{x,\mathrm{min}}$ is the lower bound of the power-law behavior. The approximate standard error σ_α of α can be derived from the width of the likelihood maximum as

$$\sigma_\alpha = \frac{\alpha - 1}{\sqrt{N}}.$$

The lowerbound $z_{x,\mathrm{min}}$ of the power law is chosen such that the following norm is minimized

$$D = \max_{x \geq z_{x,\mathrm{min}}} |F_d(x) - F(x)|,$$

where $F_d(x)$ and $F(x)$ are the cumulative function of the data and the power law, respectively. In Fig. 7, we show the tail behavior of the experimentally measured data (black circles) in logarithmic and linear scales. The curve represents the approximation in the form of Eq. (8) with the tail coefficient α computed by Eq. (9) and shown in Fig. 8(b).

V. STOCHASTIC MODELING OF VELOCITY FLUCTUATIONS

Various Lagrangian stochastic models have been developed for the description of inertial particles. We first summarize them and then explain how the models used here are different. In Maxey,[41] the gravitational settling of aerosol particles in homogeneous and stationary random flow fields is studied. Using numerical simulations of Gaussian random fields, it is shown that the coupled effect of particle inertia and flow stochasticity produces an increased settling velocity. Vasiliev and Neishtadt[42] consider the problem of finite-size particle transport in steady flows in the presence of small noise.

Reynolds[43] derive for one dimensional flows and Lagrangian stochastic models for the prediction of fluid velocities
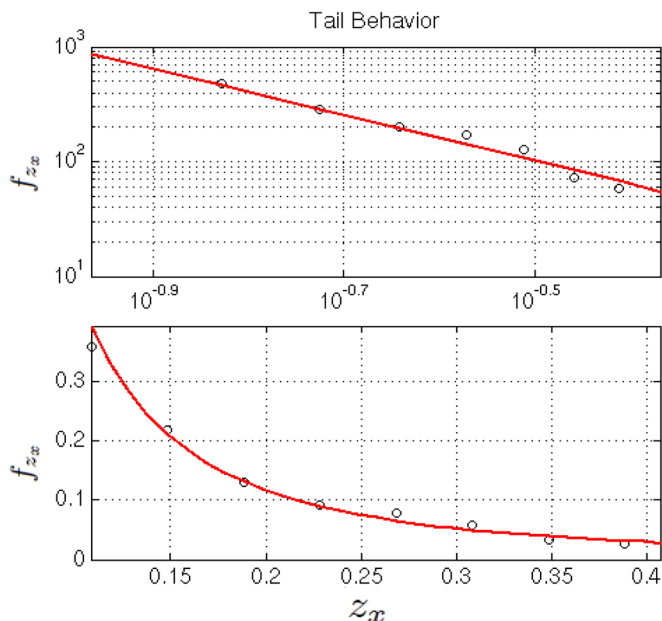

FIG. 7. (Color online) Tail behavior of the probability density function for the *x*-component velocity fluctuations (in logarithmic and linear scales); curve: analytical approximation in the form (8); black circles: histogram of the experimentally measured data.
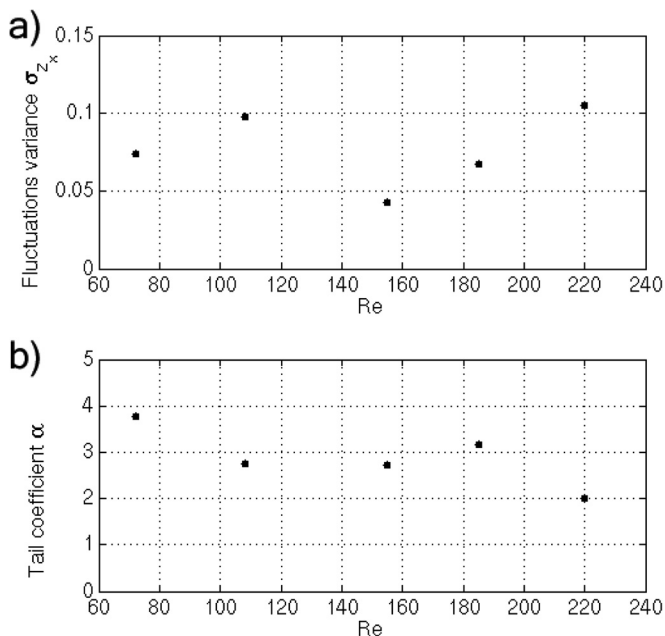

FIG. 8. (a) Standard deviation of the *x*-component of the velocity fluctuations as a function of the flow Reynolds number. (b) Tail coefficient for the statistics of the velocity fluctuations.

along heavy-particle trajectories, by assuming the well-mixed condition. This approach ensures consistency with the Eulerian fluid velocity statistics. However, for higher dimensional flows, additional assumptions are required for the unique definition of a Lagrangian stochastic model using this approach. The derived model is applied to simulate the trajectories of heavy particles in a vertical turbulent pipe flow. In Pavliotis *et al.*,[44] the problem of inertial particles in a random flow field with specified structure is considered. Specifically, the authors study the case of a time-dependent flow with stationary spatial structure and with random time dependence defined by a stationary Ornstein-Uhlenbeck process. Using homogenization theory, they prove that under appropriate assumptions, the large-scale, long-time behavior of the inertial particles is governed by an effective diffusion equation for the position variable alone.

Klyatskin and Elperin[45] and Klyatskin[46] study the problem of diffusion of a low-inertia particle in the field of a random force that is spatially homogeneous. In this case, the authors prove that the problem admits an analytic solution which predicts that the particle velocity will be a Gaussian stochastic process with known covariance function. Bec *et al.*[47,48] study the dynamics of very heavy particles suspended in incompressible flows with δ-correlated-in-time Gaussian statistics. Under these assumptions, they derive a model which is used to single out the mechanisms leading to the preferential concentration of particles.

In all of the above cases, the Lagrangian stochastic models are either derived for a specific flow with given statistical characteristics or do not include the effects of dynamical terms due to inertia such as the Basset-Boussinesq term. In what follows, we apply and evaluate three different stochastic models for the description of the random fluctuations observed in the experimental study which are specifically developed to quantify the combined effect of stochasticity

(due to incomplete dynamical modeling and flow reconstruction errors) and inertial dynamics. As we observed in Sec. IV, the measured statistics show dynamical features that cannot be justified as broadband experimental noise. To capture these dynamical features, we use stochastic models that are based on the Maxey-Riley equation but with *a priori* unknown coefficients that are determined based on the experimental observations. We assume that the deterministic model is excited by a stochastic source for which we also seek an optimal description. The goal of this study is to understand whether a stochastic model can account for the observed fluctuations and how close its (numerically computed) parameters are to the theoretical ones.

A. Maxey-Riley model with additive and multiplicative noise

The first model that we consider is a stochastic version of the Maxey-Riley equation including both additive and multiplicative white noise. The additive noise is essential to achieve a finite variance of the velocity fluctuations since, as we saw in Sec. IV, the Maxey-Riley equation predicts for this flow field zero velocity fluctuations after small amount of time. On the other hand, the multiplicative noise allows for generation, by the analytical model, of non-Gaussian statistics (heavy-tail distributions), which is also a statistical feature that we observed experimentally. Based on this discussion, we consider a model of the form

$$
d\mathbf{v} = \left[\frac{D\mathbf{U}}{Dt} - \gamma(\mathbf{v} - \mathbf{U}) \right] dt - \beta(\mathbf{v} - \mathbf{U})d\mathbf{W}_1(t; \omega) \\
+ \sqrt{2}\sigma d\mathbf{W}_2(t; \omega).
$$

(10)

Note that according to the Maxey-Riley equation, the drag coefficient is given by $\gamma = \frac{2}{3St}$. Now, by setting $\boldsymbol{\zeta} = \mathbf{v} - \mathbf{U}$ we have

$$
d\zeta = -\gamma\zeta dt - \beta\zeta d\mathbf{W}_1(t; \omega) + \sqrt{2}\sigma d\mathbf{W}_2(t; \omega). \quad (11)
$$

This last Ito stochastic differential equation is linear with constant coefficients and can be solved exactly.[49,50] In the statistically stationary regime (i.e., after the initial transient regime), we have the correlation function

$$
C_{\zeta\zeta}(\tau) = \frac{\sigma^2}{\gamma - \beta^2} \exp\left(-\left[\gamma - \beta^2\right]\tau\right), \quad (12)
$$

and the stationary probability distribution function for each of the components of the random fluctuation $\zeta = (\zeta_x, \zeta_y)$

$$
f_{\zeta_x}(x) = c\left(\beta^2 x^2 + 2\sigma^2\right)^{-\frac{\gamma}{\beta^2}+1}, \quad (13)
$$

where c is a normalization constant. Note that for $\beta^2 \to 0$, we have convergence to Gaussian statistics

$$
f_{\zeta_x}(x) \to c' \exp\left(-\frac{\gamma}{2\sigma^2}x^2\right).
$$

To determine the unknown parameters γ, β, we use the statistics obtained from the experiment in Sec. IV. More specifically, we have from Eq. (12) the correlation time scale

$$
\tau_{\zeta_x} = \frac{1}{\gamma - \beta^2}.
$$

Moreover, from the form of the probability distribution function, we have the tail coefficient expressed as

$$
\alpha = \frac{2\gamma}{\beta^2} - 2.
$$

By solving the last two equations with respect to the unknown parameters we obtain

$$
\gamma = \frac{\alpha + 2}{\tau_{\zeta_x}\alpha}, \qquad \beta^2 = \frac{2}{\tau_{\zeta_x}\alpha}.
$$

In order to determine the unknown parameter describing the intensity of the additive noise σ, we use the maximum-likelihood method directly applied to the experimental data. The values of these parameters are shown in Fig. 9 for different Re (black curve). Note that according to the stochastic Maxey-Riley equation, $\gamma = \frac{2}{3St}$ and $\beta = 0$ (light curve—red). Surprisingly, we observe that the drag coefficient has a decreasing trend as Re becomes smaller, contrary to what the theoretical expression predicts (light curve—red). In Fig. 10, we present the analytical probability density function (13) along with the experimentally measured histogram of velocity fluctuations for the case of Re = 185. We observe that both the tail behavior and the variance of the experimental distribution are captured satisfactorily by the stochastic model.

Finally in Fig. 11(a), we present a set of time series for the velocity fluctuations produced by numerically simulating the stochastic ordinary differential Equation (11). In Fig. 11(b), we present the experimentally measured time series for the same flow. We observe than even though the spread of the numerically produced fluctuations is close to the experimental one, the dynamics of the fluctuations is qualitatively different with smaller periods of oscillation in the numerical case relative to the experiment.

B. Maxey-Riley model with Basset–Boussinesq term and additive noise

To improve the dynamics of the numerically produced fluctuations, we consider a stochastic model that is based on the Maxey-Riley equation including the Basset–Boussinesq
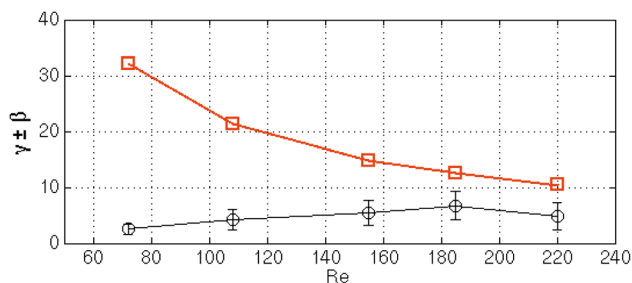
FIG. 9. (Color online) Drag coefficient γ computed by fitting the stochastic model (10) to the experimental data (black curve). The error bars indicate the intensity of the multiplicative noise β. The light curve (red) shows the theoretical value predicted by the Stokes drag.
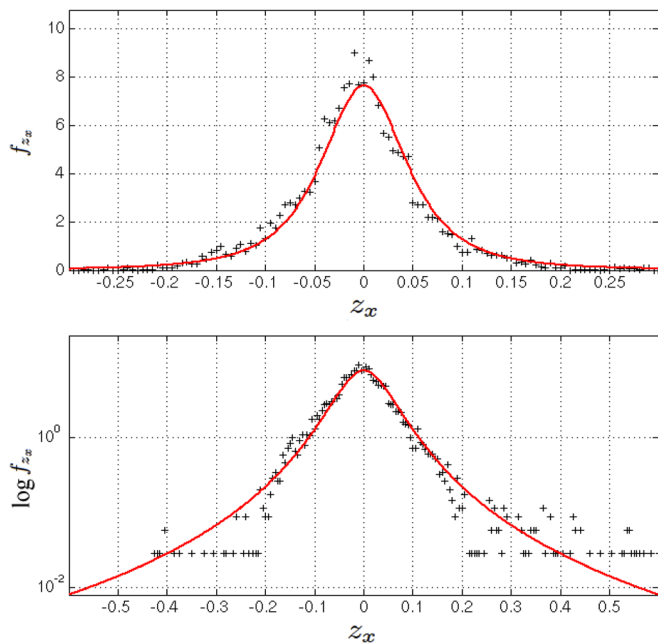
FIG. 10. (Color online) Histogram (black markers) of experimentally measured velocity fluctuations for medium-size particles and Re = 185 superimposed on the stationary probability density function (light curve—red) of the stochastic model.

integral term and excited by an additive white noise. Specifically, we consider the following stochastic model for the velocity fluctuations $\zeta = \mathbf{v} - \mathbf{U}$:

$$d\zeta = -\left(\gamma\zeta + \delta \int_0^t \frac{\dot{\zeta}(s)}{\sqrt{t-s}}\, ds\right)dt + \sqrt{2}\sigma d\mathbf{W}_2(t;\omega). \quad (14)$$

The theoretical values of the coefficients γ, δ are given by

$$\gamma = \frac{2}{3St}, \quad \delta = \sqrt{\frac{2}{\pi St}}. \quad (15)$$

The integral term included in the stochastic model (14) does not allow for analytical determination of the stochastic response. To this end, we use Monte-Carlo simulation to determine the stochastic characteristics of the response for various sets of the parameters γ, δ. Specifically, we follow Higham[51] to generate random samples for the stochastic pro-

cess $d\mathbf{W}_2(t;\omega)$ and for each random realization, we solve numerically the integrodifferential Equation (14). To identify the unknown parameters, we compute a map from (γ,δ)-parameter space to the correlation time scale of the response τ_{ζ_x}. Then we find all the possible pairs (γ,δ) that result in the experimental value τ_{z_x}.

In Fig. 12, we present the surface $\tau_{\zeta_x} = S(\gamma,\delta)$. We observe that for the limiting case of $\delta = 0$ (Maxey-Riley equation without memory term), the correlation time scale remains very small except of the region of very small drag coefficient γ (which, according to the theoretical value of γ, occurs only for the case of very large particles). As the coefficient of the memory term increases, the correlation time scale starts to increase, illustrating the contribution of the integral term to the dynamics of finite-size particles.

Using the experimental values for the correlation time scale τ_{z_x} we find the contour $S(\gamma,\delta) = \tau_{z_x}$. This is shown for the case Re = 185 as the light curve (red) in Fig. 12. In the same figure, the black solid curves indicate the theoretical values of γ, δ and their intersection (white marker) shows the theoretical value of the correlation time scale.

As Fig. 12 demonstrates for this Reynolds number, the correlation time scale predicted by the theoretical model is fairly close to the experimentally measured one. This is not the case, however, for smaller Reynolds numbers where, as it is shown in Fig. 13, there is a larger deviation between the theoretically predicted correlation time scale and the experimentally measured one. This behavior is consistent with the results of Sec. V A where we saw that larger discrepancies between theoretical values and experiment occur for low flow Reynolds numbers.

In Fig. 14, we present time series of velocity fluctuations computed by directly simulating the stochastic model (14). The parameters of the model were chosen such that $S(\gamma,\delta) = \tau_{z_x}$. Then, among all these pairs γ, δ, we chose the one that is closer to the theoretical value (white mark). Similarly with Sec. V A, we used the maximum-likelihood method to determine the noise intensity σ. As we can observe, even though the addition of the memory term improved the agreement between the experimentally measured correlation time scale and the one predicted by the theoretical model, the fluctuations produced by the model have very short period relative to those that we observe experimentally. This fact is
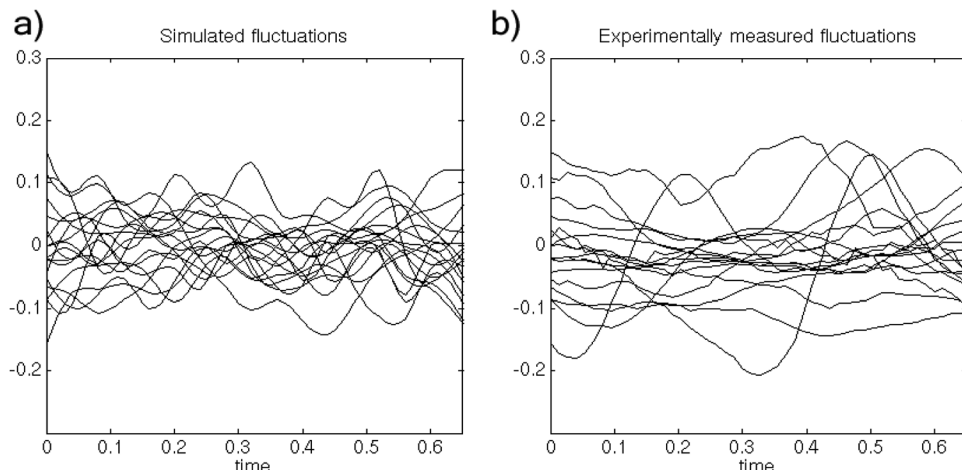

FIG. 11. Particle velocity fluctuations for Re = 185. (a) Simulated fluctuations according to the Maxey-Riley stochastic model with additive and multiplicative noise (Eq. (11)). (b) Experimentally measured fluctuations.
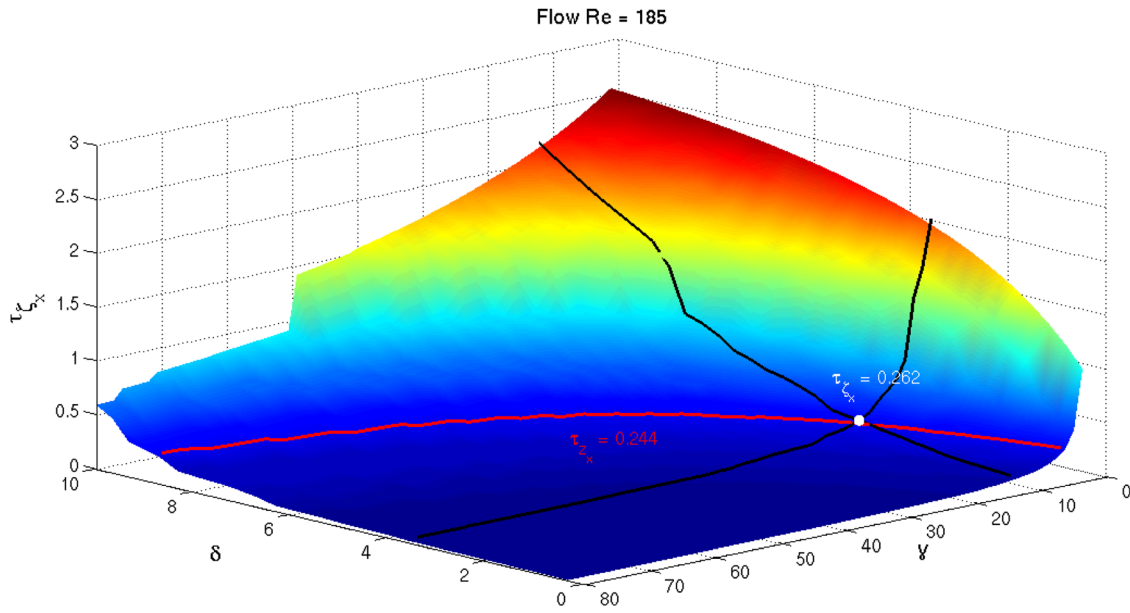
FIG. 12. (Color online) Colored surface: correlation time scale for the stochastic model (14) as a function of the drag coefficient γ and the memory coefficient δ—the color indicates the magnitude of the correlation time scale. The black curves indicate the theoretical values of the coefficients and the light curve (red) indicates the experimentally measured correlation time scale.

also illustrated by the number of zero crossings of the numerically produced time series which is much larger than in the experimental time series. To this end, we use an alternative method for the characterization of the random fluctuations based on the construction of a theoretical model that has a response with spectrum which approximates the experimentally observed.

C. Maxey-Riley model with additive colored noise

The third stochastic model that we consider is based on the Maxey-Riley equation excited by colored noise whose statistical characteristics are determined from the experimental measurements. Our analysis is based on the spectral properties of the velocity fluctuations. As we saw in Sec. IV, an analytical form of the spectrum that satisfactorily captures the experimental one is given by Eq. (7). Here, we derive an analytical model that can reproduce this spectral form and we also determine its coefficients based on the experimental observations.

We first explain why the memory term cannot reproduce the output spectrum observed experimentally, which lead us
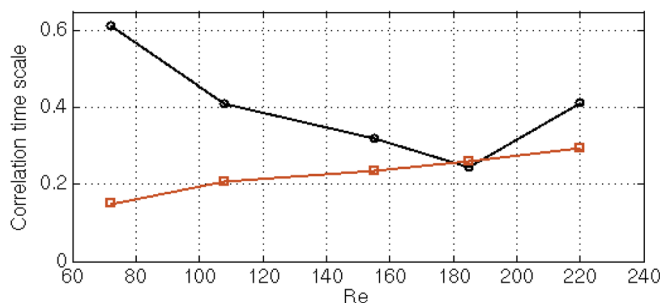

FIG. 13. (Color online) Correlation time scale measured experimentally (black curve) and according to the generalized Maxey-Riley coefficients (see Eq. (4) or (15)) (light curve—red).

to the consideration of colored excitation noise. We consider the Maxey-Riley equation with Basset-Boussinesq term

$$\dot{\zeta} = -\gamma\zeta - \delta\int_0^t \frac{\dot{\zeta}(s)}{\sqrt{t-s}}\,ds + \sqrt{2}\sigma\mathbf{F}(t).$$

After a sufficiently long time (so that the transient effects due to initial conditions have decayed), the last equation is linear and time invariant. Therefore, we can perform spectral analysis assuming that the forcing is also a stationary process. We consider the Laplace transform of the impulse response function (the response for the case where $\mathbf{F}(t) = \delta(t)$) to obtain

$$s\mathcal{L}[z] = -\gamma\mathcal{L}[z] - \delta\mathcal{L}[z]s^{1/2} + 1,$$

so

$$\mathcal{L}[z] = \frac{1}{s + \sqrt{\pi}\delta s^{1/2} + \gamma}.$$

We are interested in the long time behavior. Hence, we consider the transfer function $H(\omega) = \mathcal{L}[z]_{s=i\omega}$ to obtain

$$H(\omega) = \frac{\sqrt{2}\sigma}{i\omega + \frac{\sqrt{2\pi}}{2}(i+1)\delta|\omega|^{1/2} + \gamma}.$$

With the assumption that the external excitation $\mathbf{F}(t)$ is white noise, we obtain the form of the output spectrum for the velocity fluctuations

$$S_{\zeta\zeta}(\omega) = |H(\omega)|^2.1 = \frac{2\sigma^2}{\left[\omega + \frac{\sqrt{2\pi}}{2}\delta|\omega|^{1/2}\right]^2 + \left[\frac{\sqrt{2\pi}}{2}\delta|\omega|^{1/2} + \gamma\right]^2}$$

$$= \frac{2\sigma^2}{\omega^2 + \sqrt{2\pi}\delta|\omega|^{3/2} + \pi\delta^2|\omega| + \sqrt{2\pi}\gamma\delta|\omega|^{1/2} + \gamma^2}.$$
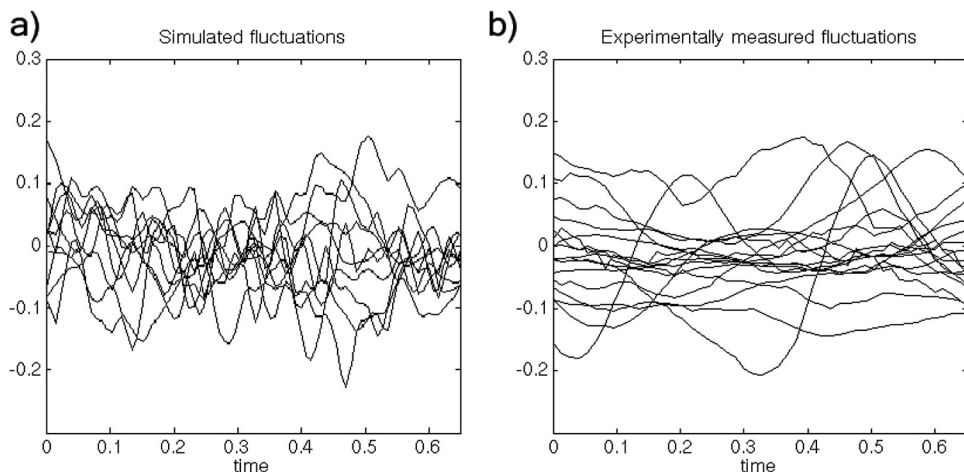
FIG. 14. Particles velocity fluctuations for Re = 185. (a) Simulated fluctuations according to the Maxey-Riley stochastic model with Basset–Boussinesq term and additive noise (Eq. (14)). (b) Experimentally measured fluctuations.

This power spectrum decays very slowly (i.e., $\mathcal{O}(\omega^{-2})$) in order to capture the decay of the experimentally measured spectrum (which decays as $\mathcal{O}(\omega^{-4})$). Moreover, the consideration of different kernels inside the integral term cannot improve this spectrum decay property.

This leads us to the conclusion that the excitation noise must be colored. To this end, we consider the next simplest form of an input spectrum given by

$$S_F(\omega) = \frac{1}{1 + i\lambda\omega}.$$

Moreover, we consider the Maxey-Riley equation without the memory term, i.e., the model

$$\dot{\zeta} = -\gamma\zeta + \sqrt{2}\sigma\mathbf{F}(t). \tag{16}$$

A spectral analysis of the last equation gives

$$S_{\zeta\zeta}(\omega) = \frac{2\sigma^2}{\gamma^2 + \omega^2}\frac{1}{1 + \lambda^2\omega^2},$$

which is consistent with the analytical form (7) that approximates the experimentally measured spectrum well. The unknown coefficients σ, λ, and γ can be determined algebraically by identifying the two spectra

$$\sigma^2 = \frac{1}{2}\frac{a_2 + \sqrt{a_2^2 - 4a_1a_3}}{2a_1a_3}, \quad \lambda^2 = 2a_1\sigma^2, \quad \gamma^2 = 2a_3\sigma^2. \tag{17}$$

In Fig. 15(a), we present the drag coefficient computed using the algebraic relations (17) (black curve) and the Stokes drag expression (15) (light curve—red). We observe that contrary to the two previous methods, this approach gives very good agreement between the theoretical value of the Stokes drag and the drag value obtained using the experimental data and the stochastic model (16) for all the Reynolds numbers considered. In the same figure, we also present the parameters for the colored input noise. We observe that for lower Reynolds number, the noise becomes more narrow-banded (larger λ) and more intense as well (larger σ).

In Fig. 16, we present time series samples for the velocity fluctuations using the stochastic model (16) and directly

measured from the experiment for Re = 185. We note that this approach results in random samples which, compared to the two stochastic approaches presented previously, are much closer qualitatively to those that are experimentally measured.

Thus, based on these results, we conclude that the Maxey-Riley equation with Stokes drag is a suitable model for the description of the random, correlated dynamics observed experimentally in the motion of finite-sized particles. We emphasize, however, that the observed behavior is a result of the excitation of the deterministic Maxey-Riley equation by a colored noise with spectrum $S_{\zeta\zeta}$ whose parameters must be determined experimentally. This input spectrum becomes energetically active over a larger band of frequencies as the flow Reynolds becomes larger. Additionally, it is more intense for the case of low flow Reynolds number,
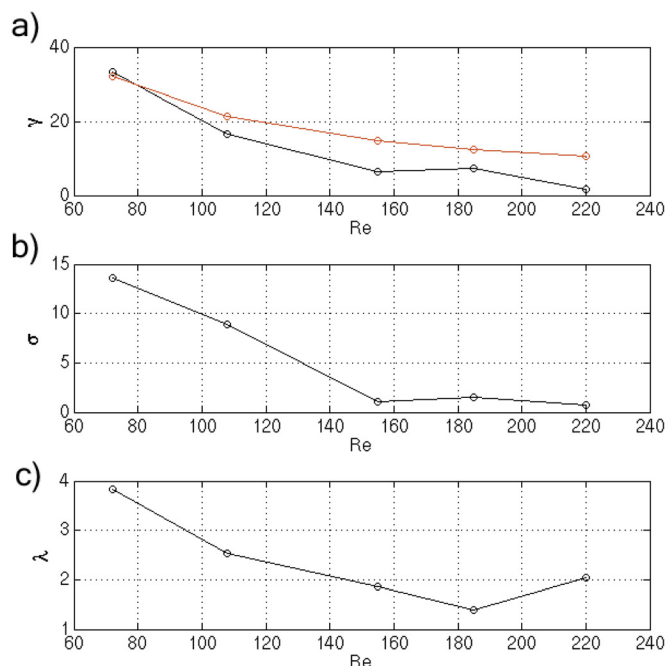

FIG. 15. (Color online) (a) Drag coefficient computed theoretically using the Maxey-Riley coefficients (15) (light curve—red) and by identifying the experimental and theoretical spectrum (Eq. (17)) in the Maxey-Riley stochastic model with additive colored noise (black curve); coefficients σ (b) and λ (c) for the stochastic model (16).
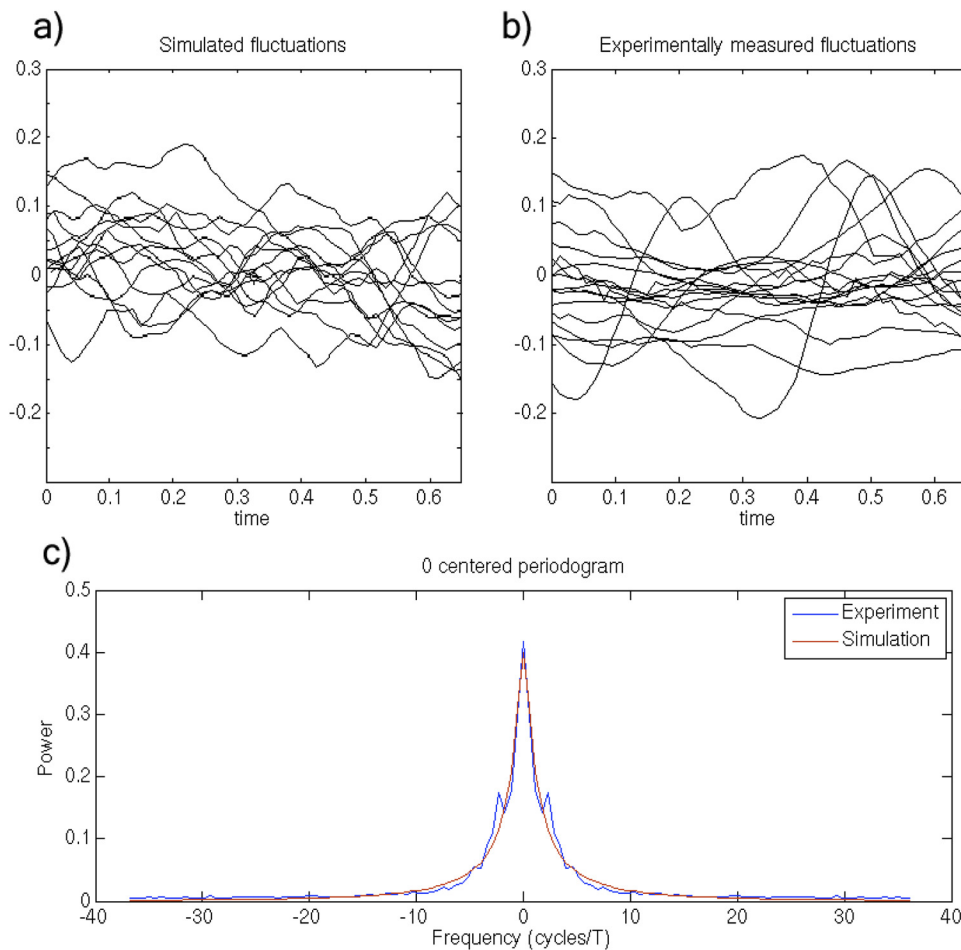
FIG. 16. (Color online) Particles velocity fluctuations for (a) Simulated fluctuations according to the Maxey-Riley stochastic model with additive colored noise (Eq. (16)) for $\mathrm{Re} = 185$. (b) Experimentally measured fluctuations. (c) Experimentally measured spectrum (dark curve—blue) and its analytical approximation (light curve—red).

where the drag coefficient becomes larger in accordance with the theoretical predictions.

VI. CONCLUSIONS

We use the experimental data to perform a direct evaluation of dynamical models describing the motion of neutrally buoyant inertial particles. In contrast to previous studies where only the ensemble statistics of the particles are compared, in this work, we compare the velocity of individual particles, measured experimentally, with the velocity obtained through various deterministic and stochastic models. Our analysis is not only restricted to the comparison of the magnitude of the velocity fluctuations but also takes into account the dynamical character of these fluctuations through suitably chosen dynamical descriptors. Following this approach, we illustrate that even relative Reynolds numbers Re_r as low as $\mathcal{O}(0.1)$ (see Figure 3) can be sufficient to cause fluctuations of the velocity of the finite-sized particles around the velocity predicted by the deterministic models (Maxey-Riley equation and its variants). These fluctuations cannot be captured by deterministic terms in the generalized Maxey-Riley equation such as the Basset-Boussinesq term, the lift force, or the Faxén corrections. Moreover, a statistical analysis of these fluctuations reveals that they cannot be due to broadband experimental noise since they present strongly correlated statistics with narrow banded spectra. Based on the statistical form of these discrepancies, we argue that

these are instead caused by poorly sampled locations of the flow field as well as by dynamical effects neglected in the modeling equations.

The next step of our analysis involves the stochastic modeling of these random, correlated fluctuations. After a detailed description of their statistics, we formulate three stochastic models that generalize the Maxey-Riley equation. The first model is based on the Maxey-Riley equation excited by parametric and additive white noises, suitably formulated to capture the non-Gaussian tail of the experimentally observed distribution, as well as the correlation time scale of the measured time series for the velocity fluctuations. In the second model, we include the Basset-Boussinesq term and additive noise, while the third model was the Maxey-Riley equation excited by colored noise with *a priori* unknown parameters that were determined by identifying the output spectrum of the model with the one that is experimentally measured. Using the spectrum identification approach, we achieve both qualitative agreement of the time series for the velocity fluctuations in theory and experiment, and also near agreement between the theoretically predicted Stokes drag coefficient and the one obtained by using the stochastic model and the experimental data. Therefore, this spectral based, stochastic generalization of the Maxey-Riley equation is a substantially better approach compared with the first two, suitable for the efficient description of the experimentally observed random fluctuations of the velocity of finite-size particles.

ACKNOWLEDGMENTS

APPENDIX: NUMERICAL SOLUTION OF THE INTEGRODIFFERENTIAL EQUATION (4)

We consider the following form of an integrodifferential equation:

$$\dot{\mathbf{z}}(t) = -\rho \int_0^t \frac{\dot{\mathbf{z}}(s)}{\sqrt{t-s}}\,ds - \tilde{M}(t)\mathbf{z}(t) + \mathbf{F}(t).$$

In what follows, we describe a central difference scheme that also takes into account the singularity of the kernel. Specifically, we consider a grid of time instants $\{t_i\}_{i=1}^n$ with equal distance from each other. Then the values $\mathbf{z}_i = \mathbf{z}(t_i)$, $\tilde{M}_i = \tilde{M}(t_i)$, and $\mathbf{F}_i = \mathbf{F}(t_i)$ are calculated on the nodes of the grid $\{t_i\}_{i=1}^n$ and the values $\dot{\mathbf{z}}_i = \dot{\mathbf{z}}(t_i')$ are calculated on the nodes of the grid $\{t_i'\}_{i=1}^{n-1}$, where $t_i' = \frac{t_{i+1}+t_i}{2}$. Therefore, we have the general relation

$$\mathbf{z}_{i+1} = \mathbf{z}_i + \dot{\mathbf{z}}_i \Delta t, \quad i = 1, ., n-1. \tag{A1}$$

Moreover, using a Crank-Nickolson implicit scheme for the time derivative, we have ($i = 1, \ldots, n-1$)

$$\dot{\mathbf{z}}_i = -\frac{\rho}{2}\left(\int_0^{t_{i+1}} \frac{\dot{\mathbf{z}}(s)}{\sqrt{t_{i+1}-s}}\,ds + \int_0^{t_i} \frac{\dot{\mathbf{z}}(s)}{\sqrt{t_i-s}}\,ds\right)$$
$$-\frac{1}{2}\left(\tilde{M}_i \mathbf{z}_i + \tilde{M}_{i+1}\mathbf{z}_{i+1}\right) + \frac{1}{2}(\mathbf{F}_{i+1} + \mathbf{F}_i).$$

Next, we focus on the calculation of the improper integrals. We decompose the improper integral into a part that can be determined numerically and a small remainder close to the singularity that we integrate analytically. Therefore, using the rectangle rule, for the first integral, we have

$$\int_0^{t_{i+1}} \frac{\dot{\mathbf{z}}(s)}{\sqrt{t_{i+1}-s}}\,ds = \int_0^{t_i} \frac{\dot{\mathbf{z}}(s)}{\sqrt{t_{i+1}-s}}\,ds + \int_{t_i}^{t_{i+1}} \frac{\dot{\mathbf{z}}(s)}{\sqrt{t_{i+1}-s}}\,ds$$
$$= \sum_{j=1}^{i-1} \frac{\dot{\mathbf{z}}_j \Delta t}{\sqrt{t_{i+1}-t_j'}} + \dot{\mathbf{z}}_i \int_{t_i}^{t_{i+1}} \frac{1}{\sqrt{t_{i+1}-s}}\,ds$$
$$= \sum_{j=1}^{i-1} \frac{\dot{\mathbf{z}}_j \Delta t}{\sqrt{t_{i+1}-t_j'}} + 2\dot{\mathbf{z}}_i \sqrt{\Delta t}.$$

For the second integral, we have

$$\int_0^{t_i} \frac{\dot{\mathbf{z}}(s)}{\sqrt{t_i-s}}\,ds = \int_0^{t_{i-1}} \frac{\dot{\mathbf{z}}(s)}{\sqrt{t_i-s}}\,ds + \int_{t_{i-1}}^{t_i} \frac{\dot{\mathbf{z}}(s)}{\sqrt{t_i-s}}\,ds$$
$$= \sum_{j=1}^{i-2} \frac{\dot{\mathbf{z}}_j \Delta t}{\sqrt{t_i-t_j'}} + \dot{\mathbf{z}}_{i-1} \int_{t_{i-1}}^{t_i} \frac{1}{\sqrt{t_i-s}}\,ds$$
$$= \sum_{j=1}^{i-2} \frac{\dot{\mathbf{z}}_j \Delta t}{\sqrt{t_i-t_j'}} + 2\dot{\mathbf{z}}_{i-1} \sqrt{\Delta t}.$$

Hence, we obtain

$$\dot{\mathbf{z}}_i = -\frac{\rho}{2}\left(\sum_{j=1}^{i-1} \frac{\dot{\mathbf{z}}_j(s)\Delta t}{\sqrt{t_{i+1}-t_j'}} + 2\dot{\mathbf{z}}_i\sqrt{\Delta t} + \sum_{j=1}^{i-2} \frac{\dot{\mathbf{z}}_j(s)\Delta t}{\sqrt{t_i-t_j'}} + 2\dot{\mathbf{z}}_{i-1}\sqrt{\Delta t}\right)$$
$$-\frac{1}{2}\left(\tilde{M}_i \mathbf{z}_i + \tilde{M}_{i+1}\mathbf{z}_{i+1}\right) + \frac{1}{2}(\mathbf{F}_{i+1} + \mathbf{F}_i).$$

Now, the last equation can also be written as

$$\dot{\mathbf{z}}_i\left(1 + \rho\sqrt{\Delta t}\right)$$
$$= -\frac{\rho}{2}\left(\sum_{j=1}^{i-1} \frac{\dot{\mathbf{z}}_j \Delta t}{\sqrt{t_{i+1}-t_j'}} + \sum_{j=1}^{i-2} \frac{\dot{\mathbf{z}}_j \Delta t}{\sqrt{t_i-t_j'}} + 2\dot{\mathbf{z}}_{i-1}\sqrt{\Delta t}\right)$$
$$-\frac{1}{2}\left(\tilde{M}_i \mathbf{z}_i + \tilde{M}_{i+1}\mathbf{z}_{i+1}\right) + \frac{1}{2}(\mathbf{F}_{i+1} + \mathbf{F}_i),$$

or equivalently,

$$\mathbf{z}_{i+1}\left(1 + \rho\sqrt{\Delta t}\right) = \mathbf{z}_i\left(1 + \rho\sqrt{\Delta t}\right)$$
$$-\frac{\Delta t \rho}{2}\left(\sum_{j=1}^{i-1} \frac{\dot{\mathbf{z}}_j \Delta t}{\sqrt{t_{i+1}-t_j'}} + \sum_{j=1}^{i-2} \frac{\dot{\mathbf{z}}_j \Delta t}{\sqrt{t_i-t_j'}} + 2\dot{\mathbf{z}}_{i-1}\sqrt{\Delta t}\right)$$
$$-\frac{\Delta t}{2}\left(\tilde{M}_i \mathbf{z}_i + \tilde{M}_{i+1}\mathbf{z}_{i+1}\right) + \frac{\Delta t}{2}(\mathbf{F}_{i+1} + \mathbf{F}_i).$$

Thus,

$$\left(\left(1 + \rho\sqrt{\Delta t}\right)\tilde{I} + \frac{\Delta t}{2}\tilde{M}_{i+1}\right)\mathbf{z}_{i+1} = \mathbf{z}_i\left(1 + \rho\sqrt{\Delta t}\right)$$
$$-\frac{\Delta t \rho}{2}\left(\sum_{j=1}^{i-1} \frac{\dot{\mathbf{z}}_j \Delta t}{\sqrt{t_{i+1}-t_j'}} + \sum_{j=1}^{i-2} \frac{\dot{\mathbf{z}}_j \Delta t}{\sqrt{t_i-t_j'}} + 2\dot{\mathbf{z}}_{i-1}\sqrt{\Delta t}\right)$$
$$-\frac{\Delta t}{2}\left(\tilde{M}_i \mathbf{z}_i\right) + \frac{\Delta t}{2}(\mathbf{F}_{i+1} + \mathbf{F}_i)$$

from which we determine $\mathbf{z}_{i+1}$, and subsequently, we obtain $\dot{\mathbf{z}}_i$ using Eq. (A1).

[1]V. Etyemezian, S. Ahonen, D. Nikolic, J. Gillies, H. Kuhns, D. Gillete, and J. Veranth, "Deposition and removal of fugitive dust in the arid southwestern united states: Measurements and model results," J. Air Waste Manage. Assoc. **54**, 1099 (2004).

[2]J. A. Hubbard, J. S. Haglund, and O. A. Exekoye, "Simulation of the evolution of particle size distributions containing coarse particulate in the atmospheric surface layer with a simple convection-diffusion-sedimentation model," Atmos. Environ. **43**, 4435 (2009).

[3]M. Y. Tsai, K. Elgethun, J. Ramaprasad, M. G. Yost, A. S. Felsot, V. R. Hebert, and R. A. Fenske, "The Washington aerial spray drift study: Modeling pesticide spray drift deposition from an aerial application," Atmos. Environ. **39**, 6194 (2005).

[4]G. Falkovich, A. Fouxon, and M. G. Stepanov, "Acceleration of rain initiation by cloud turbulence," Nature **419**, 151 (2002).

[5]M. Pinsky and A. Khain, "Turbulence effects on droplets growth and size distribution in clouds—A review," J. Aerosol Sci. **28**, 1177 (1997).

[6]R. A. Shaw, "Particle turbulence interactions in atmospheric clouds," Annu. Rev. Fluid Mech. **35**, 183 (2003).

[7]D. Lewis and T. Pedley, "Planktonic contact rates in homogeneous isotropic turbulence: Theoretic predictions and kinematic simulations," J. Theor. Biol. **205**, 377 (2000).

[8]B. J. Rothschild and T. R. Osborn, "Small scale turbulence and plankton contact rates," J. Plankton Res. **10**, 465, (1988).

[9]A. Bracco, P. Chavanis, A. Provenzale, and E. A. Spiegel, "Particle aggregation in a turbulent Keplerian flow," Phys. Fluids **11**, 2280 (1999).

[10]I. dePater and J. Lissauer, *Planetary Science* (Cambridge University Press, Cambridge, England, 2001).

[11]P. Tanga, A. Babiano, B. Dubrulle, and A. Provenzale, "Forming planetesimals in vortices," Icarus **121**, 158 (1996).

[12]S. Weidenschilling, "Aerodynamics of solid bodies in the solar nebula," Month. Not. R. Astron. Soc. **180**, 57 (1977).

[13]G. G. Stokes, "On the effect of the internal friction of fluid on the motion of pendulums," Trans. Cambridge Philos. Soc. **9**, 8 (1851).

[14]C. W. Oseen, "Uber die stokessche formel und uber die verwandte aufgabe in der hydrodynamic," Ark. Mat., Astron. Fys. **6**, 29 (1910).

[15]I. Proudman and J. R. A. Pearson, "Expansions at small Reynolds number for the flow past a sphere and circular cylinder," J. Fluid Mech. **2**, 237 (1957).

[16]T. Sano, "Unsteady flow past a sphere at low Reynolds number," J. Fluid Mech. **112**, 433 (1981).

[17]P. G. Saffman, "The lift on a small sphere in a slow shear flow," J. Fluid Mech. **22**, 340 (1965).

[18]A. B. Basset, *A Treatise on Hydrodynamics* (Deighton Bell, London, UK, 1888).

[19]N. Mordant and J.-F. Pinton, "Velocity measurement of a settling sphere," Eur. Phys. J. B **18**, 343 (2000).

[20]C. J. Lawrence and R. Mei, "Long-time behavior of the drag on a body in impulsive motion," J. Fluid Mech. **283**, 301 (1995).

[21]M. R. Maxey and J. J. Riley, "Equation of motion for a small rigid sphere in a nonuniform flow," Phys. Fluids **26**, 883 (1983).

[22]N. M. Qureshi, M. Bourgoin, C. Baudet, A. Cartellier, and Y. Gagne, "Turbulent transport of material particles: An experimental study of finite size effects," Phys. Rev. Lett. **99**, 184502 (2007).

[23]R. D. Brown, Z. Warhaft, and G. A. Voth, "Acceleration statistics of neutrally buoyant spherical particles in intense turbulence," Phys. Rev. Lett. **103**, 194501 (2009).

[24]G. A. Voth, A. la Porta, A. M. Crawford, J. Alexander, and E. Bodenschatz, Measurement of particle accelerations in fully developed turbulence," J. Fluid Mech. **469**, 121 (2002).

[25]E. Calzavarini, R. Volk, M. Bourgoin, E. Leveque, J.-F. Pinton, and F. Toschi, "Acceleration statistics of finite-sized particles in turbulent flow: The role of Faxen forces," J. Fluid Mech. **630**, 179 (2009).

[26]N. T. Ouellette, P. J. J. O'Malley, and J. P. Gollub, "Transport of finite-sized particles in chaotic flow," Phys. Rev. Lett. **101**, 174504 (2008).

[27]N. T. Ouellette and J. P. Gollub, "Dynamic topology in spatiotemporal chaos," Phys. Fluids **20**, 064104 (2008).

[28]N. T. Ouellette and J. P. Gollub, "Curvature fields, topology, and the dynamics of spatiotemporal chaos," Phys. Rev. Lett. **99**, 194502 (2007).

[29]D. Vella and L. Mahadevan, "The cheerios effect," Am. J. Phys. **73**, 817 (2005).

[30]G. K. Batchelor, *An Introduction to Fluid Dynamics* (Cambridge University Press, Cambridge, England, 2000).

[31]K. L. Henderson, D. R. Gwynllyw, and C. F. Barenghi, "Particle tracking in Taylor-Couette flow," Eur. J. Fluid Mech. **26**, 738 (2007).

[32]A. Babiano, J. H. Cartwright, O. Piro, and A. Provenzale, "Dynamics of a small neutrally buoyant sphere in a fluid and targeting in Hamiltonian systems," Phys. Rev. Lett. **84**, 25 (2000).

[33]T. P. Sapsis and G. Haller, "Instabilities in the dynamics of neutrally buoyant particles," Phys. Fluids **20**, 017102 (2008).

[34]E. Mechaelides, "A novel way of computing the Basset term in unsteady multiphase flow computations," Phys. Fluids A **4**, 1579 (1992).

[35]M. A. T. van Hinsberg, J. H. M. ten Thije Boonkkamp, and H. J. H. Clercx, "An efficient, second order method for the approximation of the Basset history force," J. Comput. Phys. **230**, 1465 (2011).

[36]F. A. Bombardelli, A. E. Gonzalez, and Y. I. Nino, "Computation of the particle Basset force with a fractional-derivative approach," J. Hydraul. Eng. **37**, 1513 (2008).

[37]P. Alexander, "High order computation of the history term in the equation of motion for a spherical particle in a fluid," J. Sci. Comput. **21**, 129 (2004).

[38]R. Mei, R. J. Adrian, and T. J. Hanratty, "Particle dispersion in isotropic turbulence under Stokes drag and Basset force with gravitational settling," J. Fluid Mech. **225**, 481 (1991).

[39]V. Armenio and V. Fiorotto, "The importance of the forces acting on particles in turbulent flows," Phys. Fluids **13**, 2437 (2001).

[40]K. Sobczyk, *Stochastic Differential Equations* (Kluwer Academic, Dordrecht, 1991).

[41]M. R. Maxey, "The gravitational settling of aerosol particles in homogeneous turbulence and random flow fields," J. Fluid Mech. **174**, 441 (1987).

[42]A. A. Vasiliev and A. I. Neishtadt, "Regular and chaotic transport of impurities in steady flows," Chaos **4**, 673 (1994).

[43]A. M. Reynolds, "On the formulation of Lagrangian stochastic models for heavy-particle trajectories," J. Colloid Interface Sci. **232**, 260 (2000).

[44]G. A. Pavliotis, A. M. Stuart, and K. C. Zygalakis, "Homogenization for inertial particles in a random flow," Commun. Math. Sci. **5**, 507 (2007).

[45]V. I. Klyatskin and T. Elperin, "Diffusion of low-inertia particles in a field of random forces and the Kramers problem," Izvestiya, Atmospheric and Oceanic Physics. **38**, 6 (2002).

[46]V. I. Klyatskin, *Stochastic Equations Through the Eye of the Physicist* (Elsevier Publishing Company, Amsterdam, The Netherland, 2005).

[47]J. Bec, M. Cencini, and R. Hillerbrand, "Heavy particles in incompressible flows: The large Stokes number asymptotics," Physica D **226**, 11 (2007).

[48]J. Bec, M. Cencini, R. Hillerbrand, and K. Turitsyn, "Stochastic suspensions of heavy particles," Physica D **237**, 2037 (2008).

[49]M. Gitterman, *The Noisy Oscillator: The First Hundred Years, from Einstein Until Now* (World Scientific, Singapore, 2005).

[50]D. Henderson and P. Plaschko, "Stochastic Differential Equations in Science and Engineering (World Scientific, Singapore, 2006).

[51]D. J. Higham, "An algorithmic introduction to numerical simulation of stochastic differential equations," SIAM Rev. **43**, 525 (2001).